ENVIRONMENTAL RESEARCH
LETTERS

LETTER

Satellite-detected large CO_2 release in southwestern North America during the 2020–2021 drought and associated wildfires

Hui Chen[1], **Wei He**[2,3,*], **Jinxiu Liu**[1], **Ngoc Tu Nguyen**[4], **Frédéric Chevallier**[5], **Hua Yang**[6,*], **Yiming Lv**[1], **Chengcheng Huang**[1], **Christian Rödenbeck**[7], **Scot M Miller**[8], **Fei Jiang**[2], **Junjie Liu**[9], **Matthew S Johnson**[10], **Sajeev Philip**[11], **Zhiqiang Liu**[12], **Ning Zeng**[13,14], **Sourish Basu**[14,15] and **David F Baker**[16]

[1] School of Information Engineering, China University of Geosciences, Beijing 100083, People's Republic of China
[2] International Institute for Earth System Science, Nanjing University, Nanjing, Jiangsu 210023, People's Republic of China
[3] Zhejiang Carbon Neutral Innovation Institute, Zhejiang University of Technology, Hangzhou, Zhejiang 310014, People's Republic of China
[4] State Key Laboratory of Hydrology-Water Resources and Hydraulic Engineering, College of Hydrology and Water Resources, Hohai University, Nanjing 210024, People's Republic of China
[5] Laboratoire des Sciences du Climat et de L'Environnement, LSCE/IPSL, CEA-CNRS-UVSQ, Université Paris-Saclay, 91191 Gif-sur-Yvette, France
[6] State Key Laboratory of Remote Sensing Science Jointly Sponsored by Aerospace Information Research Institute of Chinese Academy of Sciences and Beijing Normal University, Faculty of Geophysical Science, Beijing Normal University, Beijing 100875, People's Republic of China
[7] Max Planck Institute for Biogeochemistry, Jena, Germany
[8] Whiting School of Engineering, Johns Hopkins University, Baltimore, MD 21211, United States of America
[9] Jet Propulsion Laboratory, California Institute of Technology, Pasadena, CA, United States of America
[10] Earth Science Division, NASA Ames Research Center, Moffett Field, CA, United States of America
[11] Centre for Atmospheric Sciences, Indian Institute of Technology Delhi, New Delhi, India
[12] CMA Key Open Laboratory of Transforming Climate Resources to Economy, Chongqing Institute of Meteorological Sciences, Chongqing 401147, People's Republic of China
[13] Laboratory of Numerical Modeling for Atmospheric Sciences & Geophysical Fluid Dynamics, Institute of Atmospheric Physics, Chinese Academy of Sciences, Beijing, People's Republic of China
[14] Earth System Science Interdisciplinary Center, College Park, MD, United States of America
[15] NASA Goddard Space Flight Center, Global Modeling and Assimilation Office, Greenbelt, MD, United States of America
[16] Cooperative Institute for Research in the Atmosphere, Colorado State University, Fort Collins, CO, United States of America
* Authors to whom any correspondence should be addressed.

E-mail: weihe@nju.edu.cn and yh_crs@bnu.edu.cn

Keywords: land carbon uptake, CO_2 emission, atmospheric inversion, carbon observatory–2, CO_2 column concentration, drought and wildfires

Supplementary material for this article is available online

OPEN ACCESS

RECEIVED
31 December 2023

REVISED
24 March 2024

ACCEPTED FOR PUBLICATION
10 April 2024

PUBLISHED
30 April 2024

Abstract

Southwestern North America (SWNA) continuously experienced megadroughts and large wildfires in 2020 and 2021. Here, we quantified their impact on the terrestrial carbon budget using net biome production (NBP) estimates from an ensemble of atmospheric inversions assimilating *in-situ* CO_2 and Carbon Observatory–2 (OCO-2) satellite XCO_2 retrievals (OCO-2 v10 MIP Extension), two satellite-based gross primary production (GPP) datasets, and two fire CO_2 emission datasets. We found that the 2020–2021 drought and associated wildfires in SWNA led to a large CO_2 loss, an ensemble mean of 95.07 TgC estimated by the satellite inversions using both nadir and glint XCO_2 retrievals (LNLG) within the OCO-2 v10 MIP, greater than 80% of SWNA's annual total carbon sink. Moreover, the carbon loss in 2020 was mainly contributed by fire emissions while in 2021 mainly contributed by drought impacts on terrestrial carbon uptake. In addition, the satellite inversions indicated the huge carbon loss was mainly contributed by fire emissions from forests and grasslands along with carbon uptake reductions due to drought impacts on grasslands and shrublands. This study provides a process understanding of how some droughts and following wildfires affect the terrestrial carbon budget on a regional scale.

1. Introduction

Terrestrial ecosystems significantly reduce the rise of CO_2 in the atmosphere and the rate of global warming by offsetting around a quarter of the world's anthropogenic CO_2 emissions (Friedlingstein *et al* 2022). There is growing evidence that human-caused global warming will increase extreme weather and climate events (Houghton 2014). In extreme drought events, warm and dry atmospheric conditions coinciding with precipitation deficits greatly exacerbate soil moisture (SM) loss (Green *et al* 2019, De Kauwe *et al* 2019), lowering the ability of terrestrial ecosystems to store carbon (Smith *et al* 2020) by affecting photosynthesis, causing an increase in tree mortality, and causing crop failure (Beillouin *et al* 2020).

Large-scale droughts have affected many areas of the world in recent decades (Ciais *et al* 2005, Gatti *et al* 2014), including North America (Zhao and Running 2010, Wolf *et al* 2016, Luo *et al* 2017). Southwestern North America (SWNA, 30–45° N, 105–125° W) has experienced one of the worst hot droughts ever documented between the summers of 2020 and 2021 (Dannenberg *et al* 2022, Williams *et al* 2022). Droughts are main climate extremes for regulating interannual variations of terrestrial carbon uptake at regional scales (Qiu *et al* 2020). With future drought and heat events expected to increase (Meehl and Tebaldi 2004, Zacharias *et al* 2014), understanding the response of terrestrial ecosystems to drought events is crucial for predicting the fate of terrestrial carbon sinks and future climate. Recently, several studies have paid attention on the impact of the southwest U.S. droughts in 2020 and (or) 2021 on terrestrial photosynthesis or gross primary production (Dannenberg *et al* 2022, Feldman *et al* 2023, Li *et al* 2023, Zhang *et al* 2023), yet none of them studied the impact of the full 2020–2021 event on the terrestrial net carbon uptake, which would potentially provide a more completed picture about the response of its ecosystem carbon sequestration to this event.

Atmospheric CO_2 inversions offer large-scale constrained estimates on the dynamic of terrestrial net carbon uptake, which could offer more objective impact assessment than using unconstrained terrestrial biosphere model simulations (He *et al* 2023a, 2023b). *In-situ* CO_2 measurements or spaceborne column-averaged CO_2 dry air molar fraction (XCO_2) retrievals provide top-down constraints on the net carbon exchange between the atmosphere and terrestrial ecosystems from regional to global scales, thus providing an opportunity to study how large-scale carbon fluxes respond to warm and dry climate features under arid conditions (Liu *et al* 2017, Sun *et al* 2017). With more spatial and temporal coverage relative to *in-situ* CO_2 measurements, satellite XCO_2 retrievals show great potential for quantifying the dynamics of regional carbon fluxes (Detmers *et al* 2015, Bowman *et al* 2017, Kwon *et al* 2021, Philip *et al* 2022), despite uncertainties in absolute net flux estimates (Feng *et al* 2016). In addition, satellite-based observations of solar-induced chlorophyll fluorescence (SIF) could provide effective constraint on gross primary production (GPP), allowing for a better understanding of the key carbon cycle processes (Li and Xiao 2019).

In this study, we investigated the impact of the 2020–2021 hot droughts and associated wildfires on the carbon cycle in SWNA using the net biome production (NBP) estimates from atmospheric inversions of *in-situ* CO_2 and Carbon Observatory 2 (OCO-2) satellite XCO_2 retrievals from the OCO-2 v10 Model Intercomparison Project (MIP) Extension, two GPP datasets derived from remote sensing-based data driven models, and two fire CO_2 emission datasets. We aimed to answer the following questions: what are the impacts of the 2020 and 2021 drought and associated wildfires on the regional carbon budgets in SWNA, how do the main driving processes (GPP, respiration, and fire emission) contribute to the carbon budget anomalies, and how about the contributions from different ecosystems?

2. Data and methods

2.1. OCO-2 v10 model intercomparison project

The OCO-2 MIP is a collaboration among atmospheric CO_2 modelers to study the impact of assimilating OCO-2 retrieval data into atmospheric inversion models. The OCO-2 v10 MIP used NASA's operational bias-corrected OCO-2 L2 Lite XCO_2 product v10r retrievals (Byrne *et al* 2023, Kiel *et al* 2019; https://daac.gsfc.nasa.gov). All models were run following a unified protocol, in which they were required to use a same input of assimilated OCO-2 XCO_2 data, data uncertainties, and anthropogenic emissions (e.g. for v10 the ODIAC 2020 was used), but could independently adopt other prior estimates of surface carbon fluxes (NEE, ocean, and fire emissions) (Crowell *et al* 2019, Peiro *et al* 2022). The outputs cover the time period 2015–2020. Here we used an extended version of OCO-2 v10, which followed the same protocol as v10 MIP but extended through the year 2021. In the OCO-2 v10 MIP Extension, 8 models are included. The detailed information about these models is shown in table 1.

The estimated fluxes from this intercomparison project have been thoroughly verified and analyzed for continental carbon budgets over the globe (Byrne *et al* 2023). The MIP has different inversion experiments assimilating various types of observational constraints, and here we used results from three experiments, including (a) IS: assimilation of *in situ* CO_2 measurements from international observing networks; (b) LNLG: assimilation of OCO-2 ACOS v10 terrestrial nadir and terrestrial glint XCO_2 retrievals; (c) LNLGIS: Assimilation of

Table 1. Configuration of each simulation used in the OCO-2 v10 MIP Extension.

Model	Institution	Transport model	Meteorology	Meteorology resolution (degree)	Prior biosphere flux	Inverse method	References
AMES	NASA Ames	GEOS-Chem	MERRA2	4° × 5°	CASA-GFED4.1 s	4D-Var	Philip *et al* (2019, 2022)
Baker	CSU	PCTM	MERRA2	1° × 1.25° prior, 4° × 5° opt	CASA- GFED3	4D-Var	Baker *et al* (2006, 2010)
CAMS	LSCE	LMDz	ERA5	1.9° × 3.75°	ORCHIDEE	Variational	Chevallier *et al* (2005, 2019)
CMS-Flux	NASA JPL	GEOS-Chem	MERRA2	4° × 5°	CARDAMOM	4D-Var	Liu *et al* (2021)
COLA	IAPCAS	GEOS-Chem	MERRA2	4° × 5°	VEGAS	EnKF	Liu *et al* (2022)
GCASv2	Nanjing Univ.	MOZART	GEOS-5	2.5° × 1.875°	BEPS	EnKF	Jiang *et al* (2021), He *et al* (2023b)
JHU	JHU	GEOS-Chem	MERRA2	4° × 5°	CASA GFED4.1s	GIM	Chen *et al* (2021a, 2021b), Miller *et al* (2020)
TM5-4DVAR	Univ. Maryland	TM5	ERA-Interim	2° × 3°	SiBCASA	4D-Var	Basu *et al* (2013, 2018)

in situ CO_2 measurements and OCO-2 ACOS v10 terrestrial nadir and terrestrial glint XCO_2 retrievals.

2.2. Common atmospheric CO_2 inversions using *in-situ* data

For comparison, we included the flux estimates from four common global atmospheric CO_2 inversions using *in-situ* data, including CAMS, Jena CarboScope, NOAA CarbonTracker (CT), and NISMON-CO_2.

The operational CAMS *in-situ* inversion assimilates measurements from ground-based CO_2 air samples (Chevallier *et al* 2019). The inversion uses a suite of prior estimates of CO_2 surface fluxes (including a climatology of terrestrial biosphere fluxes simulated by the ORCHIDEE model) and uses the LMDz model to represent atmospheric transport driven by the ERA5 horizontal wind fields. The variational formulation of Bayes' theorem is used in the inversion. The CAMS CO_2 inversion release version v21r1 (hereafter referred to as CAMS-surface; 1979–2021) were used. We used monthly averages of the NBP with a geographical resolution of 1° × 1° for this analysis. The CAMS official product v21r1 is not identical to the CAMS product in the MIP ensemble, which imposed a unique processing of the satellite retrievals, a unique database for air-sample measurements and a unique prior fossil fuel emission database. The CAMS official product also benefits from a dedicated quality assurance and quality control process, while the MIP had its own.

The Jena CarboScope inversion (www.bgcjena.mpg.de/CarboScope/?ID=s10oc_v2022; (Rödenbeck *et al* 2003)) provides gridded a posteriori NBP flux estimates that constrained by *in-situ* CO_2 measurements. In comparison to CAMS, it differs significantly in many aspects, including the priori information and its error structure, the atmospheric transport model, and the assimilated observations. The CarboScope inversion consistently assimilated a fixed number of stations for each version throughout the entire study period. We utilized the s10oc_v2022 version (abbreviated as Jena_s10oc), which assimilated data from 78 surface stations spanning the period of 2010–2021. The spatial resolution of the TM3 transport model used in the CarboScope inversion is 3.75° × 5°, with optimized daily fluxes.

We utilized the most recent NBP estimates from the NOAA CT inversions, which comprise the CT2022 release (Jacobson *et al* 2023a) extended by the CT Near-Real Time (CT-NRT) release CT-NRT.v2023-4 (Jacobson *et al* 2023b). The fluxes for the ocean and land biosphere were optimized by estimating weekly scaling factors for 156 ecoregions spanning the globe. These scaling factors multiplied prior fluxes from upstream biosphere model simulations, and optimization was conducted via a 600-member ensemble of TM5 transport simulations (Krol *et al* 2005) using a 12-week windowed ensemble Kalman filter. Wildfire and fossil-fuel CO_2 emissions were predetermined. On the other hand, the CT-NRT system uses prior fluxes obtained from a statistical flux anomaly model, which is driven by anomalies of temperature, sunlight, and precipitation, along with the climatology of optimized fluxes from CT2022. Moreover, the CT-NRT simulations are designed to use fewer and provisional CO_2 measurement data from the near-real time CO_2 ObsPack product (Schuldt *et al* 2022). CT was initially introduced by Peters *et al* (2005) and has since undergone continuous improvement. The standard CT (CT2022) provides monthly 1°× 1° global fluxes over the period 2000–2020, and CT-NRT.v2023-4 provides similar fluxes over the years 2021 and 2022. It is extensively documented and evaluated at https://carbontracker.noaa.gov/.

The NISMON-CO2 (v2022.1) inversion optimizes surface CO_2 fluxes in accordance with atmospheric observations using the 4D-Var algorithm (Niwa *et al* 2022) and the NICAM-TM transport model (Tomita and Satoh 2004). In NISMON-CO_2 ver. 2021.1, the fossil fuel emission data were from the GCP-GridFED ver. 2021.2 (Jones *et al* 2021), and the land use and biosphere fluxes were from the VISIT model (Ito and Inatomi 2012). The biomass burning emission data were obtained from the Global Fire Emissions Database (GFED) ver. 4.1s (Van Der Werf *et al* 2017), and the air–sea CO_2 exchange data were obtained from the JMA (Iida *et al* 2021). The observational data were derived from the ObsPack-NRT and the ObsPack-GLOBALVIEWplus (Masarie *et al* 2014). Additionally, other independently provided data, specifically versions 6.1_2021_03-01 (Schuldt *et al* 2021a) and 6.1.1_2021-05-17 (Schuldt *et al* 2021b) of ObsPack-GLOBALVIEWplus and ObsPack-NRT were utilized, respectively. NISMON-CO2 (v2022.1) provides monthly $1° \times 1°$ global fluxes spanning the period 1990–2021.

2.3. Satellite-based GPP datasets

Two satellite data-driven GPP-based models GOSIF GPP (Li and Xiao 2019) and FluxSat (Joiner *et al* 2018) were used in this study. The first model is the Orbiting Carbon Observatory-2 (OCO-2) global SIF dataset, or GOSIF, and its biome-specific linear relationships with observed GPP. The GOSIF-GPP dataset (Version 2) was estimated using a data-driven model in which variables reflecting vegetation conditions, meteorological conditions, and land cover information are used as model inputs. A more refined SIF product based on the OCO-2 (GOSIF) derivation uses the strong linear relationship between GPP and GOSIF to generate the GOSIF GPP dataset. It has been widely applied to describe the spatial and temporal variability of GPP and the response of GPP to climate change on a regional or global scale (Constenla-Villoslada *et al* 2022, Zhao *et al* 2022). To make the analyses more robust, we employed another GPP dataset, FluxSat (Version 2), which is derived through a data-driven approach that relies on FLUXNET measurements and reflectance in the seven spectral bands of the Moderate Resolution Imaging Spectroradiometer (MODIS), and is calibrated against FLUXNET measurements (Joiner and Yoshida 2020). In the analyses, we used the average of GOSIF GPP and FluxSat GPP due to their high consistence.

2.4. Biomass burning emissions

The monthly biomass burning (BB) emissions data from the GFEDv4 and Fire Energetics and Emissions Research version 1.0 (FEERv1) (Ichoku and Ellison 2013) were used. GFEDv4 is an industry-standard global emissions model that provides 3-hourly, daily, and monthly estimates of global emissions for 42 species at 0.25° spatial resolution since 1997 (Giglio *et al* 2013, Wees *et al* 2022). GFED is based on the Carnegie–Ames–Stanford Approach (CASA) biogeochemical model, which simulates carbon fluxes through satellite-based observations of vegetation, weather, burned area, and burn integrity. FEERv1 is based on the fire radiative power (FRP) method and is obtained at a 0.1° spatial grid resolution. It uses the time integration of FRP remote sensing measurements, allowing a more direct estimation of biomass burning rates and bypassing some of the uncertainties in biogeochemical simulations required by the burning zone approach. Here, due to the possible uncertainty in BB estimates, we combined GFEDv4 and FEERv1 data for the analyses, which will make our analyses more reliable. We found the two datasets have a high agreement in SWNA, thus used the average of them in the analyses.

2.5. Ancillary data

To characterize climate and vegetation growth conditions during the 2020–2021 drought event, an array of ancillary data was employed. These data include precipitation and air temperature metrological reanalysis data, standardized precipitation evapotranspiration index (SPEI), satellite soil moisture (SM) and fraction of absorbed photosynthetically active radiation (FAPAR).

The precipitation and air temperature data were taken from the fifth generation European Reanalysis (ERA5), which is produced by the European Centre for Medium-Range Weather Forecasts (ECMWF) (Hersbach *et al* 2020). This dataset is provided at a spatial resolution of 0.25° and a monthly time-step.

The SPEI data were obtained from the global SPEI database (SPEIbase v2.8), which provides long-term information on global drought conditions with a spatial resolution of 0.5° and a monthly temporal resolution. It has a multiscale character, providing SPEI time scales between 1 and 48 months. The time scale of SPEI used in this study was 12 months. The SPEI is designed to take into account both precipitation and potential evapotranspiration (PET) in determining drought (Vicente-Serrano *et al* 2010). Thus, unlike the SPI, the SPEI captures the main impact of increased temperatures on water demand. When the SPEI value is less than or equal to -0.5, drought is considered to have occurred, and a smaller value indicates a higher drought severity.

The root-zone SM from the Global Surface Evaporation Amsterdam Method (GLEAM v3.6a) (Martens *et al* 2016) was used to characterize soil moisture stress or drought. The GLEAM root-zone SM (v3.6a) was generated by the satellite surface soil moisture product ESA-CCI SM (v02.5) through a

data assimilation scheme (Martens *et al* 2016). We used the monthly averaged SM at a spatial resolution of 0.25°.

FAPAR is a key parameter for vegetation photosynthesis and primary production estimation (Claverie *et al* 2016). In this study, Global land surface satellite (GLASS) FAPAR products were used. GLASS FAPAR is approximated as one minus PAR transmittance across the canopy, which can be calculated from GLASS LAI and other variables (Xiao *et al* 2015). The GLASS FAPAR from MODIS data is an instantaneous value at 10:30 a.m. local time, which is very close to the daily average FAPAR. The spatial resolution of the raw GLASS FAPAR data is 0.05° and the temporal resolution is 8 day, and was resampled to the monthly scale in this study.

2.6. Calculation of terrestrial carbon flux components

NBP is a net signal generated by different biogeochemical processes such as total primary productivity (GPP), heterotrophic respiration (Rh) and fire disturbances. Their relative contributions to interannual and long-term carbon cycle variability may differ (Zeng *et al* 2005, Ahlström *et al* 2015). Therefore, more efforts are needed to quantify which components contribute most to interannual variability in NBP and to correct for average state changes. In this study, NBP is mainly used to study the response of terrestrial ecosystems to extreme drought events. A negative sign of NBP indicates the release of carbon to the atmosphere while a positive sign indicates the uptake of carbon from the atmosphere. The carbon balance of terrestrial ecosystems can be expressed by the following equation:

$$\mathrm{NBP} = \mathrm{GPP} - \mathrm{Reco} - \mathrm{BB} = \mathrm{NEP} - \mathrm{BB} \quad (1)$$

where NEP represents net ecosystem productivity, BB represents disturbances such as wildfire, harvesting, grazing, and land cover change, and Reco is the total ecosystem respiration. We decompose the NBP anomalies during the 2020 and 2021 droughts into their different constituent fluxes.

In this study, we used the average BB data based on the burning region GFEDv4 and the FRP-based FEERv1 for calculating the BB anomaly. Reco is the difference between the average of the two GPP datasets (GOSIF GPP and Fluxsat GPP) and NEP, and the derivation equations for NEP and Reco are as follows

$$\mathrm{NEP} = \mathrm{NBP} + \mathrm{BB} \quad (2)$$

$$\mathrm{Reco} = \mathrm{GPP} - \mathrm{NBP} - \mathrm{BB}. \quad (3)$$

2.7. Calculation of anomaly

Anomalies of carbon fluxes and meteorological, hydrological and vegetation indicators were calculated as follows:

$$X_i' = X_i - \overline{X_{\mathrm{BL}}} \quad (4)$$

where X_i' denotes the anomaly of variable X in month i of a year, X_i represents the value of variable X in month i of a year, and $\overline{X_{\mathrm{BL}}}$ denotes the average of the monthly data of variable X during a benchmark period. We used the period 2015–2019 as the baseline for drought detection, since for North America this time period is similar to the long term mean and does not have any large anomalous events (https://droughtmonitor.unl.edu/NADM/TimeSeries.aspx).

3. Results and discussion

3.1. Climate anomalies in SWNA during the 2020–2021 hot drought

We firstly analyzed the hydroclimate anomalies in SWNA from a historical perspective over the period of 2010–2021, which indicate that the years of 2020 and 2021 are among the driest years (figure 1). The SPEI value in 2020 was the unprecedentedly low in 12 years, and was also among the lowest ones in 2021 (figure 1(a)). Similarly, large negative anomalies for both precipitation and SM occurred in the second half of 2020 (figure 1(b)). A clear summer-autumn drought in 2020 was identified by both SPEI and SM, while a clear spring-summer drought in 2021 was identified by SPEI, precipitation and SM (figure 1(b)). The 2020–2021 drought was characterized by lower air temperatures in spring while higher in summer and by severe deficits in precipitation and SM throughout both years (figure S1). The precipitation in 2020 declined sharply to about 43% below the average, which persisted until late 2021 (figure S1(b)). The significant decrease in precipitation led to a further scarcity of SM in winter 2020 (figures S1(c) and 1(c)), which condition continued in late summer 2021. An obvious SM drought extended from early summer 2020 to late summer 2021, accompanying abnormal high summer temperature (heatwaves), which shaped the hot droughts during the 2020–2021 period.

We also analyzed the spatial evolution of the hot drought during the period from summer 2020 to summer 2021 (figures S2 and 1(c)). Spatially, more than 60% of the region experienced positive air temperature anomalies in summer 2020 (JJA), with the largest degree of heatwaves in Arizona and New Mexico. In autumn 2020, heatwaves further expanded to California (figure S3(a)). In winter 2020, nearly 60% of the areas experienced a decrease of precipitation at 1.5 mm per day on average (figure S3(b)), which was consistent with a further exacerbation of the lack of SM spatially. Starting from May 2020, the severe meteorological drought resulted in large-scale SM deficits, when about 94% of this region experienced negative SM anomalies (figure 1(c)). This 2020 summer drought further developed in the autumn, reached its peak in the winter of 2020, continued into the spring of 2021, and started weakening during the summer of 2021. The precipitation played an

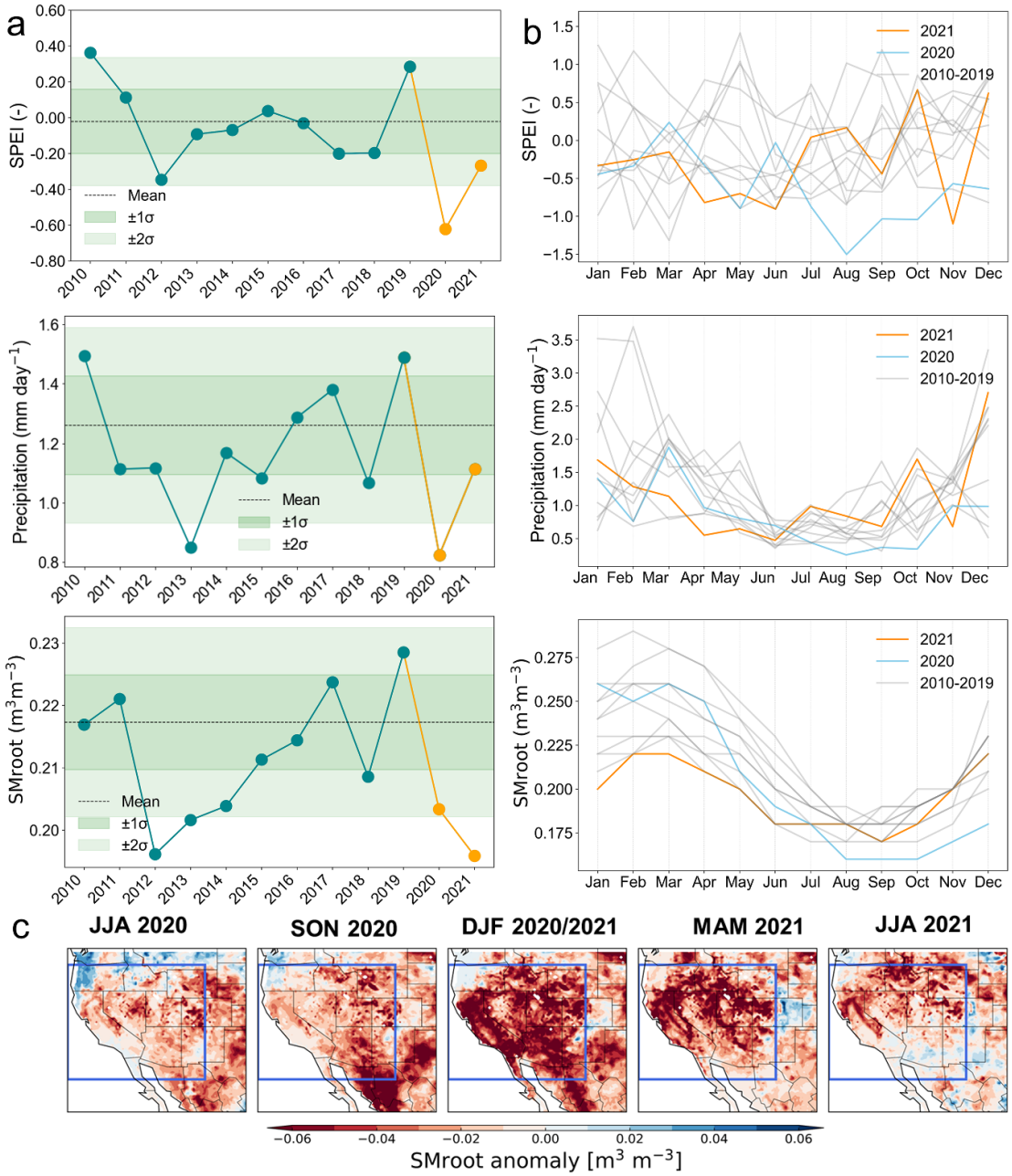

Figure 1. Drought conditions in 2020–2021. (a) Annual mean time series of 12-month scale SPEI, precipitation and root-zone soil moisture (SMroot) from 2010 to 2020; shaded bands indicate one to two standard deviations from the average for the period from 2015 to 2019. (b) Monthly variation of SPEI, precipitation, and SMroot in the SWNA area. The gray lines indicate the years from 2010 to 2019 and the color lines indicate the years of 2020 and 2021. (c) The spatial distributions of the anomalies of SMroot during June–August 2020 (JJA), September–November 2020 (SON), December–February 2020–2021 (DJF), March–May 2021 (MAM), June–August 2021 (JJA). The brown color indicates negative anomalies (decrease), while the blue color indicates positive anomalies (increase).

important role (figure S3(b)), while air temperature also contributed largely (figure S3(a)). In summary, most of SWNA experienced an intense and prolonged hydrological drought from early summer 2020 until late summer 2021.

3.2. Seasonal anomalies in vegetation growth and land carbon uptake

The 2020–2021 drought and wildfires strongly impacted vegetation growth and carbon uptake, causing dramatic reductions in FAPAR and GPP and corresponding seasonal anomalies in NBP (figure 2, tables S1–S4). Over the main drought period (June 2020–August 2021), FAPAR and GPP suffered from continuous declines with the lowest in September 2020 and May–June 2021, respectively (figures 2(a) and (b)). Accordingly, there were similar NBP reductions indicated by the OCO-2 MIP inversions (figures 2(d)–(f)), suggesting apparent carbon releases. In the MIP inversions, all posterior estimates revealed much stronger NBP anomalies than that shown in the prior (figure 2(c)), as well as more

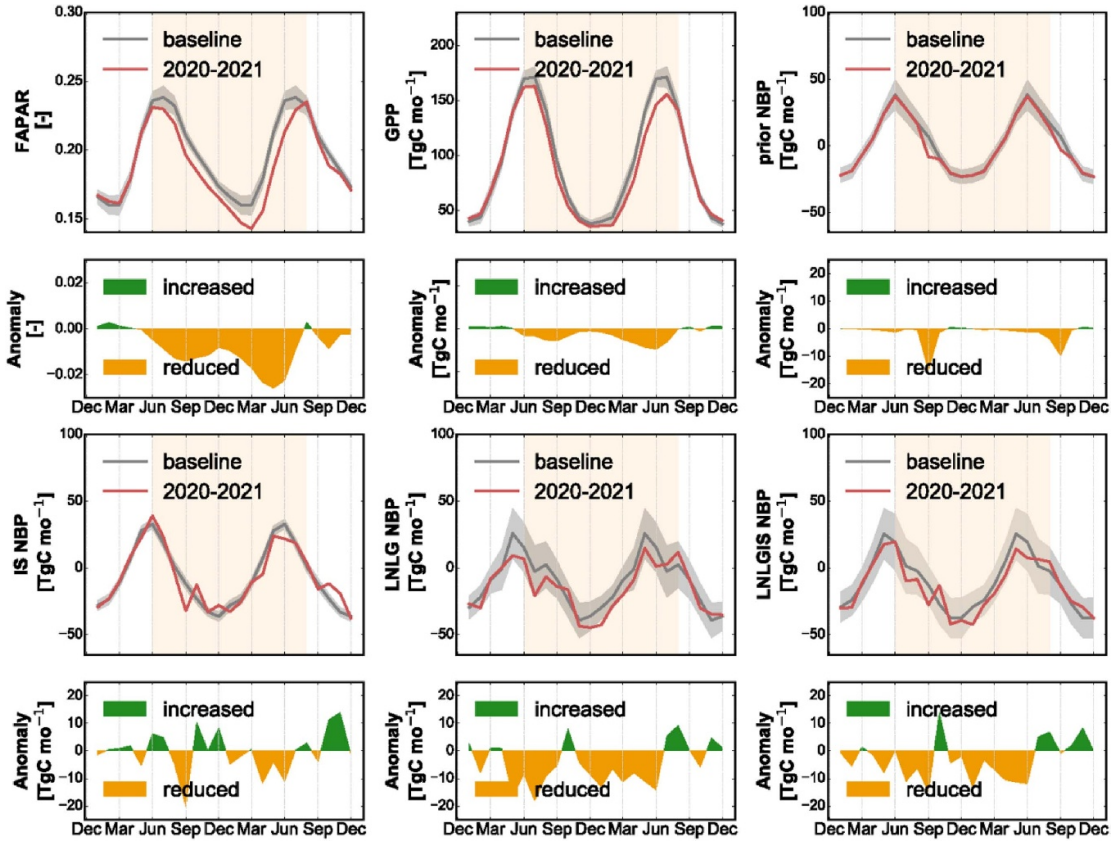

Figure 2. Seasonal variations and anomalies in FAPAR, GPP, and NBP over SWNA during 2020–2021 relative to the period of 2015–2019. The NBP estimates were from the prior and posteriors (IS, LNLG and LNLGIS) of the inversions within the OCO-2 v10 MIP Extension project. The shadowed orange areas indicate the core time period for drought onset.

consistent timing with the reductions in FAPAR and GPP. Such clear NBP reductions in both years were also revealed by the CAMS, Jena CarboScope and NISMON inversions; a clear NEP reduction in 2021 was revealed by CarbonTracker while not for 2020, which could result from the unique feature of CT-NRT by combining a statistical flux anomaly model (figure S2). It is worth noting that, all inversion estimates consistently showed a rebound in NBP after the main drought period, which may be associated with the enhancement of NEP (figure S3) induced by an improved condition in SM availability (figure S1(c)).

Spatially, the SWNA region experienced a substantial decline in FAPAR during the drought, with the most severe decrease in the west, and most of the region experienced suppressed vegetation activity in summer (figure S4(a)). A similar decline was observed for GPP, which decreased by 63% in the spring, with the most severe decrease in northwestern SWNA, followed by the northeastern part (figure S4(b)). We analyzed the spatial distribution of seasonal anomalies of NBP during the same period (figure S5). The ensemble NBP anomalies for OCO-2 v10 MIP prior were nearly neutral (figure S5) while these in the IS, LNLG, and LNLGIS experiments were apparent negative, suggesting that the *in-situ* and satellite-observed atmospheric CO_2 concentrations provided effective constraints on NBP anomalies induced by the drought and wildfire event. Specifically, the overall NBP anomalies constrained by *in-situ* CO_2 observations (IS experiment) show limited carbon uptake reductions, slightly stronger in the northern part of the SWNA, especially in 2020 SON and 2021 JJA (figure S5). The LNLG and LNLGIS NBP anomalies have roughly similar spatial patterns and show much stronger carbon uptake reductions in the southwestern part of the SWNA in 2020/2021 DJF. More specifically, the longitudinal variation in NBP anomalies suggests that the overall NBP anomalies for LNLG and LNLGIS are significantly more robust in carbon uptake reductions despite showing considerable inter-model discrepancies.

Overall, the changes in NBP estimated by the OCO-2 MIP inversions generally agree with these changes in GPP and FAPAR. They all capture the drought impacts on the terrestrial carbon uptake over SWNA. Their estimated NBP drops abruptly in September 2020 (figures 2(d)–(f)), when a severe wildfire event occurred (figures S7 and S8). During summer 2021, there was also a large CO_2 release due to wildfires.

3.3. Event-induced changes of the regional annual carbon budget

The total carbon budget anomalies in the SWNA region during 2020–2021 were analyzed. Firstly, we

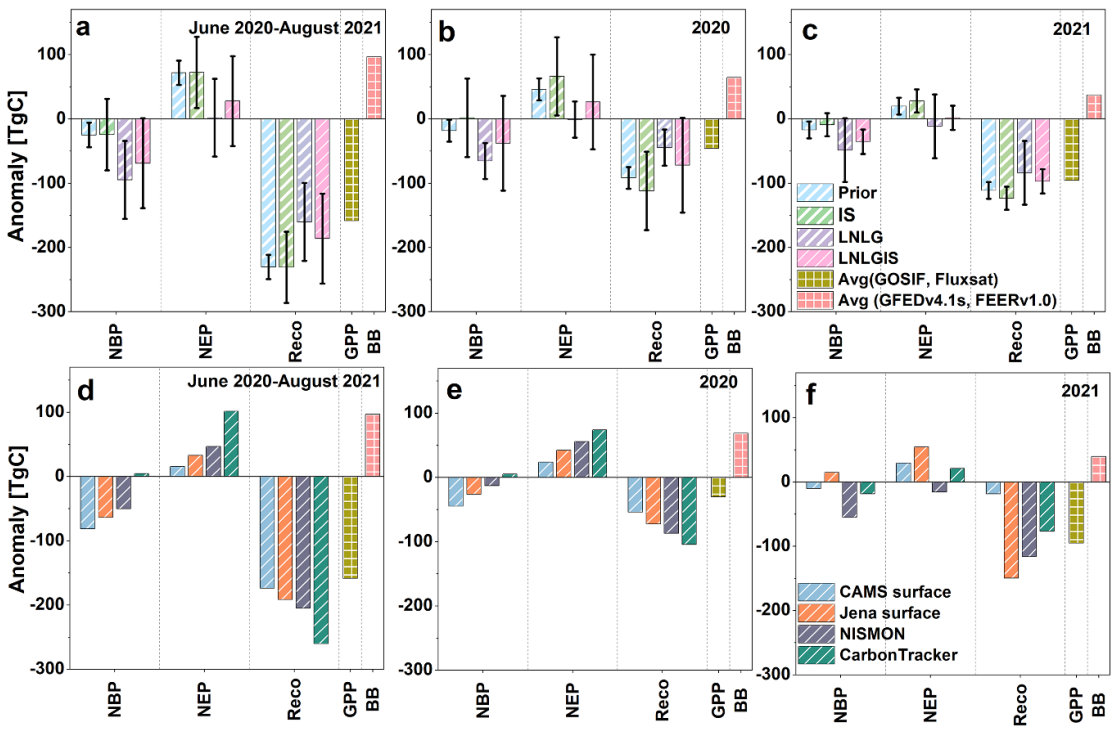

Figure 3. Anomalies of NBP and relevant fluxes in SWNA during 2020–2021. (a)–(c) OCO-2 MIP results, including PRIOR, IS, LNLG, and LNLGIS, where the error bar indicates a standard deviation; (d)–(f) CAMS surface, Jena CarboScope, NISMON, and CarbonTracker inversions. BB indicates the biomass burning emission, which is an average of the GFEDv4 and FEERv1 estimates (the two have almost identical BB values). GPP is an average of the GOSIF and FluxSat GPP estimates (the two have almost identical GPP values).

investigated the main drought period from June 2020 to August 2021 (figure 3(a)). During this period, the regional NBP experienced a reduction revealed by the *in-situ* inversions (IS), the satellite inversions (LNLG) and the inversions constrained with both observations (LNLGIS) from the OCO-2 v10 MIP Extension project. The prior also estimated a reduction of -25.1 ± 18.9 TgC, which is comparable with the estimate of -24.5 ± 55.5 TgC in the IS inversion. Although the prior estimated a comparable size of NBP decline, its multi-year average NBP in this region indicated a carbon source, contrasting with that all the inversions pointed to a carbon sink. With the constraint of OCO-2 XCO_2 retrievals, the inverse estimates exhibited much larger absolute NBP anomalies (-95.0 ± 60.6 TgC by LNLG and -69.2 ± 69.9 TgC by LNLGIS) than the IS estimate. Despite large difference between absolute values of NBP anomalies, both the IS inversion and the satellite inversion (LNLG) estimated an annual carbon uptake loss greater than 80% (table 2). A comparable magnitude of NBP reduction was also indicated by the both surface inversions of CAMS and Jena, albeit that their multi-year average NBPs in this region indicated near carbon neutral (table 2). Also, the NISMON and CarbonTracker inversions indicated a decrease in NBP, while their multi-year average NBPs exhibited a contrasting direction in carbon sink or source. The continuous NBP decline was also found in a number of flux tower observations from the AmeriFlux network in the SWNA region (figure S8, 18 sites covering the study period), for example, at sites US-Ses (OSH), US-Seg (OSH), and US-Mpj (WSA). The NBP reduction during this event was primarily resulting from BB emission, which was as large as 96.8 TgC (figure 3(a)). Meanwhile, it was partly offset by the increase in NEP, which was slight in the satellite inversion but much larger on the surface inversion within the MIP, and was also indicated by the CAMS surface, Jena CarboScope, and NIMSON inversions (figure 3(d)). Combining the NBP estimates from different inversion models with the component flux estimates from a same set of data sources, the analyses consistently suggested that the increase in NEP resulted from a more considerable decrease in Reco (-230.41 to -160.52 TgC) than in GPP (-158.8 TgC). The larger inhibition in Reco than in GPP can also be observed at flux tower observations (figure S8), for example, at sites US-Var (GRA), US-Wjs (SAV), and US-Bi2 (CRO), where a greater suppression in respiration during some of the drought and wildfire period leading to an unexpected increase in NEP. Such unexpected phenomenon is discussed later.

Then, we assessed the anomalies in the regional carbon budgets for the full years of 2020 (figures 3(b) and (e)) and 2021 (figures 3(c) and (f)). The primary mechanisms underlying the regional carbon balance change of the two years differed markedly. In 2020, fire emissions (also known as biomass burning, BB)

Table 2. Regional NBP anomalies during the 2020–2021 drought and wildfire event.

Datasets	Baseline (TgC)	Absolute anomaly (TgC)	Relative change
OCO-2MIP Prior	102.84 ± 25.8	−25.18 ± 18.9	−24%
OCO-2 MIP IS	−28.40 ± 57.6	−24.57 ± 55.5	−87%
OCO-2 MIP LNLG	−114.11 ± 50.3	−95.07 ± 60.6	−83%
OCO-2 MIP LNLGIS	−114.58 ± 55.29	−69.21 ± 69.9	−60%
CAMS surface v21r1	0.11	−81.63	/
Jena surface s10oc_v2022	−0.05	−63.88	/
NISMON-CO2_v2022.1	−43.89	−50.33	−115%
CarbonTracker 2022	71.6	−4.55	−6%

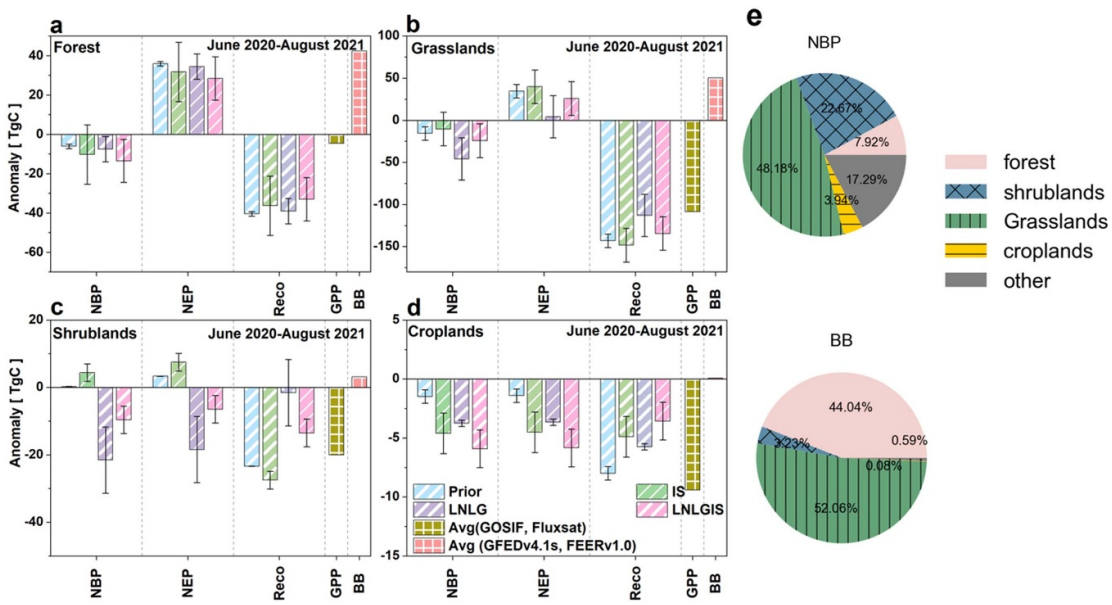

Figure 4. Anomalies of NBP and its constituent fluxes in SWNA during the June 2020–August 2021 drought. over different ecosystems. The study area was divided into different ecoregions based on the 2020 MODIS land cover data product (MOD12C1) and summarized into four types. The dominant ecosystem types include grasslands and shrublands (see figure S9).

released 68.73 TgC, but NEP increased by 34.25 TgC due to the compensation of a decline in GPP and a larger attenuation in Reco, leading to a NBP decrease by 30.16 TgC on average. In this year, the underlying processes of NEP (GPP and Reco) showed generally smaller reductions than the magnitude of fire emissions, indicating that fires dominated the carbon budget dynamics in this region. In 2021, the OCO-2 inversions consistently showed a smaller anomaly in NBP and NEP compared to 2020 while much larger reductions in both GPP and Reco. Relative to 2020, the fire emissions were apparently smaller (figure S6(c)). Thus, in 2021, the anomaly of the ecosystem carbon uptake was likely more dominant when compared to the contribution by fire emissions. Surprisingly, NEP increased in both 2020 and 2021 as Reco decreased more than GPP. In particular, Reco was substantially attenuated in 2021, allowing the increased NEP to largely compensate for the carbon losses due to wildfires. In both 2020 and 2021, GPP and Reco were greatly damped, and this attenuation was significantly larger in Reco than in GPP. These flux anomalies were also indicated by most surface inversions of CAMS, Jena, NIMSON and CarbonTracker (figures 3(e) and (f)).

To better understand the changes in purposes regional carbon budgets from the ecosystem level, we investigated the contribution of different ecosystems to the carbon balance anomalies (figure 4). The four dominant ecosystems were forests (4.06%), shrubs (17.14%), grasslands (49.61%), and crops (2.68%), with the spatial distributions shown in figure S9. Here we made statistics on the LNLG inversion result. As an arid area, most of the SWNA are covered by grass and shrubs, which are drought-vulnerable vegetation and usually contribute sizeable flux emission during droughts. Among them, drought and wildfires had a huge impact on the NBP of grasslands and shrublands, with grasslands contributing almost half of the total while forests contributed a much less proportion (only 8%, see figure 4(e)). In terms of BB contribution, forests and grasslands contributed about 44% and 52% of carbon loss, respectively. In comparison, the BB emissions by the shrubland ecosystem and the crop ecosystem were much smaller, for which the decline in NBP was mainly driven by the ecosystem

carbon uptake, i.e., NEP. The OCO-2 MIP inversions broadly showed that the event caused significant suppressions in both GPP and respiration, leading to a decrease in NEP, i.e. drought caused a decrease of NBP for the shrubland and crop ecosystems.

4. Discussion

4.1. Unexpected larger inhibition in Reco than in GPP during the 2020–2021 event

In the analyses, we noticed an unexpected larger inhibition in Reco than in GPP during the 2020–2021 event, which results in NEP increase. We noticed this phenomenon happened in both 2020 and 2021. We are aware that there existed uncertainties when deriving Reco from NBP, BB (fire emission) and GPP. To reduce such uncertainty, we employed two BB and GPP products. For NBP, a large array of datasets from both OCO-2 XCO_2 inversions and *in-situ* inversions were included. All results consistently pointed to such phenomenon, albeit of discrepancy in the anomaly magnitudes, making the finding reliable to some extent. We checked it by analyzing *in-situ* eddy flux measurements, and found this happened at some of these flux sites but not at most sites. During compound drought and fire events, there are evidence to support the occurrence of such phenomenon. The larger inhibition in Reco than in GPP could be explained by suppressed microbial soil respiration, which has also been found in previous studies in the post-drought and post-fire periods (Selsted *et al* 2012, Kopittke *et al* 2014, Chen *et al* 2019, Huang *et al* 2021). Further evidence, especially from intensive *in-situ* measurements, is critically needed to confirm this finding.

4.2. Discrepancy among the flux estimates by different inversion models

Although most inversion models have general agreement on the large carbon loss during the event, the magnitude and even the direction of flux anomalies remain differ notably (see table 2). Firstly, satellite inversions estimate higher NBP anomalies than *in-situ* based inversions do. It could be because that, the satellite inversion used vertical column CO_2 data instead of surface CO_2 data to infer carbon fluxes, in theory the column CO_2 data contain more signals than surface CO_2 did, especially the column CO_2 contain more CO_2 sources in the atmosphere, thus larger sink to balance it in an inversion framework (mass balance between sink and source). Similarly, higher estimates from satellite inversions than *in-situ* inversions were reported in previous studies about the regional carbon sinks in Europe (Feng *et al* 2016), US (Byrne *et al* 2023) and China (He *et al* 2023b). Secondly, the differences in the regional carbon budget estimates among the three OCO-2 MIP experiments and four *in-situ* based global inversions partly originate from this gap between satellite inversions and *in-situ* inversions, as well as uncertainties among different inversion frameworks (due to both inversion system design and assimilated data). To our knowledge, there are quite limited atmospheric CO_2 sites in and around SWNA, making the *in-situ* inversion less reliable, especially in a global inversion framework. In addition, the SWNA is an arid region, where vegetation signal is relative weak in a large proportion of the domain, making reliable regional flux estimate challenging. In comparison, model ensemble could provide more reliable estimates on regional flux and its anomaly, especially these constrained by satellite XCO_2 observations (He *et al* 2023a, 2023b).

4.3. Implications and future perspectives

Our study provided a comprehensive assessment on the impact of the 2020–2021 drought and associated wildfires in the SWNA on the terrestrial carbon budget using multiple datasets. Such events are widespread over the globe in the context of climate warming, calling for more research attention on this topic. We highlight that the impact of drought and post-drought (e.g. wildfires) should be considered together, as well as ecosystem recovery and resilience during the whole period, which may offer new perspectives on how terrestrial ecosystems respond to climate extremes. In addition, to better monitor the response of terrestrial ecosystems to drought and following disturbance, we need to combine measurements from different scales, for example, satellite land surface observations, eddy covariance flux observations, atmospheric CO_2 concentration observations from both *in-situ* and satellite platforms. Further efforts should also made to reduce uncertainties in fire CO_2 emission estimates, especially encouraging to conduct it within top-down inversion frameworks (van der Velde *et al* 2021, Zheng *et al* 2023).

5. Conclusions

In this study, we quantified the impact of the 2020–2021 drought in the SWNA on the terrestrial carbon budget using the NBP estimates from atmospheric inversions of *in-situ* CO_2 and OCO-2 XCO_2 retrievals, two satellite-based GPP datasets, and two fire CO_2 emission datasets. We found that the 2020–2021 drought and associated wildfires in SWNA led to a large CO_2 loss, an ensemble mean of 95.07 TgC estimated by the satellite inversions using both nadir and glint XCO_2 retrievals within the OCO-2 v10 MIP, greater than 80% of the annual total carbon sink. Furthermore, the carbon loss in 2020 was primarily driven by fire emissions, whereas in 2021, it was predominantly contributed by drought impacts on terrestrial carbon uptake. Additionally, satellite inversions revealed that the substantial carbon loss was largely attributed to fire emissions from forests and grasslands, coupled with reductions in carbon

uptake resulting from drought impacts on grasslands and shrublands. The atmospheric inversions using satellite or surface CO_2 observations reveal an unexpected larger attenuation in Reco than in GPP over SWNA during the 2020–2021 event, which largely compensates for its carbon release. Our study provides a new perspective on the response of SWNA ecosystem carbon budget to the 2020–2021 drought and associated wildfires, and an in-depth understanding of how it was impacted on a regional scale.

Data availability statement

The CAMS carbon flux data are publicly available at https://ads.atmosphere.copernicus.eu/cdsapp#!/dataset/cams-global-greenhouse-gas-inversion?tab=form. The Jena CarboScope carbon flux data are publicly available at www.bgc-jena.mpg.de/CarboScope/. The CarbonTracker carbon flux data are publicly available at http://carbontracker.noaa.gov. The NISMON-CO2 carbon flux data are publicly available at www.nies.go.jp/doi/10.17595/20201127.001-e.html. The GOSIF GPP dataset is publicly available at https://globalecology.unh.edu/data/GOSIF-GPP.html. The GLEAM v3.6a root-zone soil moisture is publicly available at www.gleam.eu/#downloads. The GLASS FAPAR dataset is publicly available at www.glass.umd.edu/Download.html. The GFED4.1s is publicly available at https://daac.ornl.gov/cgi-bin/dsviewer.pl?ds_id=1293. The FEERv1.0 dataset is publicly available at https://feer.gsfc.nasa.gov/data/emissions/.

No new data were created or analysed in this study.

Acknowledgments

This research is funded by the National Natural Science Foundation of China (Grant Nos. 42277453 and 41907378). The OCO-2 XCO_2 data are produced by the Observing Carbon Observatory project at the Jet Propulsion Laboratory, California Institute of Technology, and obtained from the data archive at the NASA Goddard Earth Science Data and Information Services Center. We acknowledge the Oak Ridge National Laboratory (ORNL) Distributed Active Archive Center (DAAC) for providing the GFED4.1s dataset and NASA Goddard Space Flight Center for providing the FEERv1.0 dataset. We also sincerely acknowledge the NOAA CarbonTracker team and the NIES NISMON team for providing inverse flux estimates, which offer essential supports to our study. Part of the research was carried out at the Jet Propulsion Laboratory, California Institute of Technology, under a contract with the National Aeronautics and Space Administration (80NM0018D0004). J L acknowledges the computational support by NASAHECC supercomputer.

ORCID iDs

Hui Chen https://orcid.org/0009-0009-4233-4424
Wei He https://orcid.org/0000-0003-0779-2496
Jinxiu Liu https://orcid.org/0009-0001-3820-8195
Ngoc Tu Nguyen https://orcid.org/0000-0003-3251-1799
Frédéric Chevallier https://orcid.org/0000-0002-4327-3813
Hua Yang https://orcid.org/0009-0009-7705-8677
Yiming Lv https://orcid.org/0009-0003-3866-6262
Chengcheng Huang https://orcid.org/0009-0000-2621-9076
Christian Rödenbeck https://orcid.org/0000-0001-6011-6249
Scot M Miller https://orcid.org/0000-0003-4462-8126
Fei Jiang https://orcid.org/0000-0003-1744-7565
Junjie Liu https://orcid.org/0000-0002-7184-6594
Matthew S Johnson https://orcid.org/0000-0002-6010-7497
Sajeev Philip https://orcid.org/0000-0002-5456-7593
Zhiqiang Liu https://orcid.org/0000-0003-2982-8381
Ning Zeng https://orcid.org/0000-0002-7489-7629
Sourish Basu https://orcid.org/0000-0001-8605-5894

References

Ahlström A *et al* 2015 The dominant role of semi-arid ecosystems in the trend and variability of the land CO_2 sink *Science* **348** 895–9

Baker D F, Bösch H, Doney S C, O'Brien D and Schimel D S 2010 Carbon source/sink information provided by column CO_2 measurements from the orbiting carbon observatory *Atmos. Chem. Phys.* **10** 4145–65

Baker D F, Doney S C and Schimel D S 2006 Variational data assimilation for atmospheric CO_2 *Tellus* B **58** 359–65

Basu S *et al* 2013 Global CO_2 fluxes estimated from GOSAT retrievals of total column CO_2 *Atmos. Chem. Phys.* **13** 8695–717

Basu S, Baker D F, Chevallier F, Patra P K, Liu J and Miller J B 2018 The impact of transport model differences on CO_2 surface flux estimates from OCO-2 retrievals of column average CO_2 *Atmos. Chem. Phys.* **18** 7189–215

Beillouin D, Schauberger B, Bastos A, Ciais P and Makowski D 2020 Impact of extreme weather conditions on European crop production in 2018 *Phil. Trans. R. Soc.* B **375** 20190510

Bowman K W *et al* 2017 Global and Brazilian carbon response to El Niño Modoki 2011–2010 *Earth Space Sci.* **4** 637–60

Byrne B *et al* 2023 National CO_2 budgets (2015–2020) inferred from atmospheric CO_2 observations in support of the global stocktake *Earth Syst. Sci. Data* **15** 963–1004

Chen J, Zhang Y, Luo Y, Zhou X, Jiang Y, Zhao J, Chen Y, Wang C, Guo L and Cao J 2019 Contrasting responses after fires of the source components of soil respiration and ecosystem respiration *Eur. J. Soil Sci.* **70** 616–29

Chen Z *et al* 2021a Five years of variability in the global carbon cycle: comparing an estimate from the orbiting carbon observatory-2 and process-based models *Environ. Res. Lett.* **16** 054041

Chen Z *et al* 2021b Linking global terrestrial CO_2 fluxes and environmental drivers: inferences from the orbiting carbon

observatory 2 satellite and terrestrial biospheric models *Atmos. Chem. Phys.* **21** 6663–80
Chevallier F, Fisher M, Peylin P, Serrar S, Bousquet P, Bréon F-M, Chédin A and Ciais P 2005 Inferring CO_2 sources and sinks from satellite observations: method and application to TOVS data *J. Geophys. Res.* **110**
Chevallier F, Remaud M, O'Dell C W, Baker D, Peylin P and Cozic A 2019 Objective evaluation of surface- and satellite-driven carbon dioxide atmospheric inversions *Atmos. Chem. Phys.* **19** 14233–51
Ciais P *et al* 2005 Europe-wide reduction in primary productivity caused by the heat and drought in 2003 *Nature* **437** 529–33
Claverie M, Matthews J L, Vermote E F and Justice C O 2016 A 30+ year AVHRR LAI and FAPAR climate data record: algorithm description and validation *Remote Sens.* **8** 263
Constenla-Villoslada S, Liu Y, Wen J, Sun Y and Chonabayashi S 2022 Large-scale land restoration improved drought resilience in Ethiopia's degraded watersheds *Nat. Sustain.* **5** 488–97
Crowell S *et al* 2019 The 2015–2016 carbon cycle as seen from OCO-2 and the global in situ network *Atmos. Chem. Phys.* **19** 9797–831
Dannenberg M P *et al* 2022 Exceptional heat and atmospheric dryness amplified losses of primary production during the 2020 U.S. Southwest hot drought *Glob. Change Biol.* **28** 4794–806
De Kauwe M G, Medlyn B E, Pitman A J, Drake J E, Ukkola A M, Griebel A, Pendall E, Prober S and Roderick M 2019 Examining the evidence for decoupling between photosynthesis and transpiration during heat extremes *Biogeosciences* **16** 903–16
Detmers R G, Hasekamp O, Aben I, Houweling S, Van Leeuwen T T, Butz A, Landgraf J, Köhler P, Guanter L and Poulter B 2015 Anomalous carbon uptake in Australia as seen by GOSAT *Geophys. Res. Lett.* **42** 8177–84
Feldman A F, Zhang Z, Yoshida Y, Gentine P, Chatterjee A, Entekhabi D, Joiner J and Poulter B 2023 A multi-satellite framework to rapidly evaluate extreme biosphere cascades: the Western US 2021 drought and heatwave *Glob. Change Biol.* **29** 3634–51
Feng L, Palmer P I, Parker R J, Deutscher N M, Feist D G, Kivi R, Morino I and Sussmann R 2016 Estimates of European uptake of CO_2 inferred from GOSAT XCO_2 retrievals: sensitivity to measurement bias inside and outside Europe *Atmos. Chem. Phys.* **16** 1289–302
Friedlingstein P *et al* 2022 Global carbon budget 2022 *Earth Syst. Sci. Data* **14** 4811–900
Gatti L V *et al* 2014 Drought sensitivity of Amazonian carbon balance revealed by atmospheric measurements *Nature* **506** 76–80
Giglio L, Randerson J T and Werf G R 2013 Analysis of daily, monthly, and annual burned area using the fourth-generation global fire emissions database (GFED4) *J. Geophys. Res.* **118** 317–28
Green J K, Seneviratne S I, Berg A M, Findell K L, Hagemann S, Lawrence D M and Gentine P 2019 Large influence of soil moisture on long-term terrestrial carbon uptake *Nature* **565** 476–9
He W *et al* 2023a Do state-of-the-art atmospheric CO_2 inverse models capture drought impacts on the European land carbon uptake? *J. Adv. Model. Earth Syst.* **15** e2022MS003150
He W *et al* 2023b Improved constraints on the recent terrestrial carbon sink over China by assimilating OCO-2 XCO_2 retrievals *J. Geophys. Res.* **128** e2022JD037773
Hersbach H *et al* 2020 The ERA5 global reanalysis *Q. J. R. Meteorol. Soc.* **146** 1999–2049
Houghton J T 2014 Climate change 2013—the physical science basis: working group i contribution to the fifth assessment report of the intergovernmental panel on climate change
Huang H, Calabrese S and Rodríguez-Iturbe I 2021 Variability of ecosystem carbon source from microbial respiration is controlled by rainfall dynamics *Proc. Natl Acad. Sci.* **118** e2115283118
Ichoku C and Ellison L T 2013 Global top-down smoke aerosol emissions estimation using satellite fire radiative power measurements *Atmos. Chem. Phys.* **14** 6643–67
Iida Y, Takatani Y, Kojima A and Ishii M 2021 Global trends of ocean CO_2 sink and ocean acidification: an observation-based reconstruction of surface ocean inorganic carbon variables *J. Oceanogr.* **77** 323–58
Ito A and Inatomi M 2012 Use of a process-based model for assessing the methane budgets of global terrestrial ecosystems and evaluation of uncertainty *Biogeosciences* **9** 759–73
Jacobson A R *et al* 2023a CarbonTracker CT2022
Jacobson A R *et al* 2023b CarbonTracker CT-NRT.v2023-4
Jiang F *et al* 2021 Regional CO_2 fluxes from 2010 to 2015 inferred from GOSAT XCO_2 retrievals using a new version of the global carbon assimilation system *Atmos. Chem. Phys.* **21** 1963–85
Joiner J and Yoshida Y 2020 Satellite-based reflectances capture large fraction of variability in global gross primary production (GPP) at weekly time scales *Agric. For. Meteorol.* **291** 108092
Joiner J, Yoshida Y, Zhang Y, Duveiller G, Jung M, Lyapustin A, Wang Y and Tucker C 2018 Estimation of terrestrial global gross primary production (GPP) with satellite data-driven models and eddy covariance flux data *Remote Sens.* **10** 1346
Jones M W, Andrew R M, Peters G P, Janssens-Maenhout G, De-Gol A J, Ciais P, Patra P K, Chevallier F and Le Quéré C 2021 Gridded fossil CO_2 emissions and related O_2 combustion consistent with national inventories 1959–2018 *Sci. Data* **8** 2
Kiel M, O'Dell C W, Fisher B, Eldering A, Nassar R, MacDonald C G and Wennberg P O 2019 How bias correction goes wrong: measurement of XCO_2 affected by erroneous surface pressure estimates *Atmos. Meas. Tech.* **12** 2241–59
Kopittke G R, Tietema A, Loon E E V and Asscheman D 2014 Fourteen annually repeated droughts suppressed autotrophic soil respiration and resulted in an ecosystem change *Ecosystems* **17** 242–57
Krol M, Houweling S, Bregman B, Van den Broek M, Segers A, Van Velthoven P, Peters W, Dentener F and Bergamaschi P 2005 The two-way nested global chemistry-transport zoom model TM5: algorithm and applications *Atmos. Chem. Phys.* **5** 417–32
Kwon M J, Ballantyne A, Ciais P, Bastos A, Chevallier F, Liu Z, Green J K, Qiu C and Kimball J S 2021 Siberian 2020 heatwave increased spring CO_2 uptake but not annual CO_2 uptake *Environ. Res. Lett.* **16** 124030
Li X, Ryu Y, Xiao J, Dechant B, Liu J, Li B, Jeong S and Gentine P 2023 New-generation geostationary satellite reveals widespread midday depression in dryland photosynthesis during 2020 western U.S. heatwave *Sci. Adv.* **9** eadi0775
Li X and Xiao J 2019 A global, 0.05-degree product of solar-induced chlorophyll fluorescence derived from OCO-2, MODIS, and reanalysis data *Remote Sens.* **11** 517
Liu J *et al* 2017 Contrasting carbon cycle responses of the tropical continents to the 2015–2016 El Niño *Science* **358** eaam5690
Liu J *et al* 2021 Carbon monitoring system flux net biosphere exchange 2020 (CMS-Flux NBE 2020) *Earth Syst. Sci. Data* **13** 299–330
Liu Z, Zeng N, Liu Y, Kalnay E, Asrar G, Wu B, Cai Q, Liu D and Han P 2022 Improving the joint estimation of CO_2 and surface carbon fluxes using a constrained ensemble Kalman filter in COLA (v1.0) *Geosci. Model Dev.* **15** 5511–28
Luo L, Apps D, Arcand S, Xu H, Pan M and Hoerling M P 2017 Contribution of temperature and precipitation anomalies to the California drought during 2012–2015 *Geophys. Res. Lett.* **44** 3184–92
Martens B, Miralles D G, Lievens H, Van Der Schalie R, De Jeu R A, Fernández-Prieto D, Beck H E, Dorigo W A and

Verhoest N E C 2017 GLEAM v3: satellite-based land evaporation and root-zone soil moisture *Geosci. Model Dev.* **10** 1903–25

Masarie K, Peters W, Jacobson A and Tans P 2014 ObsPack: a framework for the preparation, delivery, and attribution of atmospheric greenhouse gas measurements *Earth Syst. Sci. Data* **6** 375–84

Meehl G A and Tebaldi C 2004 More intense, more frequent, and longer lasting heat waves in the 21st Century *Science* **305** 994–7

Miller S M, Saibaba A K, Trudeau M E, Mountain M E and Andrews A E 2020 Geostatistical inverse modeling with very large datasets: an example from the orbiting carbon observatory 2 (OCO-2) satellite *Geosci. Model Dev.* **13** 1771–85

Niwa Y, Ishijima K, Ito A and Iida Y 2022 Toward a long-term atmospheric CO_2 inversion for elucidating natural carbon fluxes: technical notes of NISMON-CO2 v2021.1 *Prog. Earth Planet. Sci.* **9** 42

Peiro H *et al* 2022 Four years of global carbon cycle observed from the orbiting carbon observatory 2 (OCO-2) version 9 and in situ data and comparison to OCO-2 version 7 *Atmos. Chem. Phys.* **22** 1097–130

Peters W, Miller J, Whitaker J, Denning A, Hirsch A, Krol M, Zupanski D, Bruhwiler L and Tans P P 2005 An ensemble data assimilation system to estimate CO_2 surface fluxes from atmospheric trace gas observations *J. Geophys. Res.* **110** D24304

Philip S, Johnson M S, Baker D F, Basu S, Tiwari Y K, Indira N K, Ramonet M and Poulter B 2022 OCO-2 satellite-imposed constraints on terrestrial biospheric CO_2 fluxes over South Asia *J. Geophys. Res.* **127** e2021JD035035

Philip S, Johnson M S, Potter C, Genovesse V, Baker D F, Haynes K D, Henze D K, Liu J and Poulter B 2019 Prior biosphere model impact on global terrestrial CO_2 fluxes estimated from OCO-2 retrievals *Atmos. Chem. Phys.* **19** 13267–87

Qiu B, Ge J, Guo W, Pitman A J and Mu M 2020 Responses of Australian dryland vegetation to the 2019 heat wave at a subdaily scale *Geophys. Res. Lett.* **47** e2019GL086569

Rödenbeck C, Houweling S, Gloor M and Heimann M 2003 CO_2 flux history 1982–2001 inferred from atmospheric data using a global inversion of atmospheric transport *Atmos. Chem. Phys.* **3** 1919–64

Schuldt K N *et al* 2021a Multi-laboratory compilation of atmospheric carbon dioxide data for the period 1957–2019; obspack_co2_1_GLOBALVIEWplus_v6.1_2021a–03–01 (NOAA Global Monitoring Laboratory)

Schuldt K N *et al* 2021b Multi-laboratory compilation of atmospheric carbon dioxide data for the period 2020–2021b; obspack_co2_1_NRT_v6.1.1_2021b–05–17 (NOAA Earth System Research Laboratory, Global Monitoring Laboratory)

Schuldt K N, Aalto T, Andrews A, Aoki S, Apadula F, Arduini J and Baier B 2022 Multi-laboratory compilation of atmospheric methane data for the period 1983–2021; obspack_ch4_1_GLOBALVIEWplus_v5.0_2022-10-17 (NOAA Earth System Research Laboratory, Global Monitoring Laboratory)

Selsted M B, van der Linden L, Ibrom A, Michelsen A, Larsen K S, Pedersen J K, Mikkelsen T N, Pilegaard K, Beier C and Ambus P 2012 Soil respiration is stimulated by elevated CO_2 and reduced by summer drought: three years of measurements in a multifactor ecosystem manipulation experiment in a temperate heathland (CLIMAITE) *Glob. Change Biol.* **18** 1216–30

Smith N E *et al* 2020 Spring enhancement and summer reduction in carbon uptake during the 2018 drought in northwestern Europe *Phil. Trans. R. Soc.* B **375** 20190509

Sun Y *et al* 2017 OCO-2 advances photosynthesis observation from space via solar-induced chlorophyll fluorescence *Science* **358** eaam5747

Tomita H and Satoh M 2004 A new dynamical framework of nonhydrostatic global model using the icosahedral grid *Fluid Dyn. Res.* **34** 357

van der Velde I R *et al* 2021 Vast CO_2 release from Australian fires in 2019–2020 constrained by satellite *Nature* **597** 366–9

Van Der Werf G R *et al* 2017 Global fire emissions estimates during 1997–2016 *Earth Syst. Sci. Data* **9** 697–720

Vicente-Serrano S M, Beguería S and López-Moreno J I 2010 A multiscalar drought index sensitive to global warming: the standardized precipitation evapotranspiration index *J. Clim.* **23** 1696–718

Wees D V, Werf G R, Randerson J T, Rogers B M, Chen Y, Veraverbeke S, Giglio L and Morton D C 2022 Global biomass burning fuel consumption and emissions at 500-m spatial resolution based on the global fire emissions database (GFED) *Geosci. Model Dev.* **15** 8411–37

Williams A P, Cook B I and Smerdon J E 2022 Rapid intensification of the emerging southwestern North American megadrought in 2020–2021 *Nat. Clim. Change* **12** 232–4

Wolf S *et al* 2016 Warm spring reduced carbon cycle impact of the 2012 US summer drought *Proc. Natl Acad. Sci.* **113** 5880–5

Xiao Z, Liang S, Sun R, Wang J and Jiang B 2015 Estimating the fraction of absorbed photosynthetically active radiation from the MODIS data based GLASS leaf area index product *Remote Sens. Environ.* **171** 105–17

Zacharias S, Koppe C and Mücke H-G 2014 Climate change effects on heat waves and future heat wave-associated IHD mortality in Germany *Climate* **3** 100–17

Zeng N, Mariotti A and Wetzel P J 2005 Terrestrial mechanisms of interannual CO_2 variability *Glob. Biogeochem. Cycles* **19** GB1016

Zhang Y, Fang J, Smith W K, Wang X, Gentine P, Scott R L, Migliavacca M, Jeong S, Litvak M and Zhou S 2023 Satellite solar-induced chlorophyll fluorescence tracks physiological drought stress development during 2020 southwest US drought *Glob. Change Biol.* **29** 3395–408

Zhao H, Jia G, Xu X and Zhang A 2022 Contrasting responses of vegetation production to rainfall anomalies across the Northeast China Transect *J. Geophys. Res.* **127** e2022JG006842

Zhao M and Running S W 2010 Drought-induced reduction in global terrestrial net primary production from 2000 through 2009 *Science* **329** 940–3

Zheng B *et al* 2023 Record-high CO_2 emissions from boreal fires in 2021 *Science* **379** 912–7